Available online at www.sciencedirect.com

SCIENCE DIRECT®

ELSEVIER

Journal of Sound and Vibration 290 (2006) 1071–1090

JOURNAL OF SOUND AND VIBRATION

www.elsevier.com/locate/jsvi

Dynamic behavior comparison of passive hydraulic engine mounts. Part 2: Finite element analysis

J. Christopherson, G. Nakhaie Jazar*

Department of Mechanical Engineering and Applied Mechanics, North Dakota State University, Fargo, North Dakota 58105, USA

Received 4 October 2004; received in revised form 20 April 2005; accepted 6 May 2005
Available online 8 August 2005

Abstract

This paper investigates the applicability of nonlinear finite elements to the difficult task of parameter identification of the structural behavior of passive hydraulic engine mounts. By using hyperelastic constitutive relationships the incompressible nature of the rubber materials that make up the bulk of the engine mount are accurately described and the results of such analysis are used directly in previously developed lumped parameter models to fully describe the dynamic behavior of two distinct hydraulic engine mounts.

1. Introduction

This is the second of a two-part series that compares two distinctly different hydraulic engine mount designs. The first part of this series described the linear and nonlinear mathematical modeling techniques required to describe the frequency behavior of the two separate hydraulic mounts considered. This section demonstrates the nonlinear finite element modeling techniques required for component evaluation and parameter identification for the structural components of the hydraulic engine mounts analyzed in the first paper.

---

*Corresponding author. Tel.: +1 701 231 8839; fax: +1 701 231 8913.
E-mail address: reza.n.jazar@ndsu.nodak.edu (G.N. Jazar).

0022-460X/$ - see front matter © 2005 Elsevier Ltd. All rights reserved.
doi:10.1016/j.jsv.2005.05.009

Nomenclature

A	cross-sectional area
A_B	decoupler disk piston area
A_p	equivalent piston area
B_r	equivalent rubber damping coefficient
B	equivalent viscous damping coefficient
M	effective fluid column mass
K_r	upper structure stiffness
C	volumetric compliance
K	sum of inverse compliance
F_T	amplitude of transmitted force
K_{dyn}	dynamic stiffness
ϕ	phase lag
X	excitation amplitude
ω	excitation frequency
E	nonlinear coefficient
Δ	decoupler gap size
ψ	strain energy density function
I_1, I_2, I_3	invariants of the Cauchy deformation tensor
$\lambda_1, \lambda_2, \lambda_3$	principal stretch ratios

Subscripts

i	inertia track
d	decoupler
fd	floating-decoupler
dd	direct-decoupler
dyn	dynamic
sys	system
atm	atmospheric
1,2,3	fluid control volume number

Shangguan et al. have recently published literature on the finite element modeling of the hydraulic engine mounts containing a floating decoupler [1,2]. In their papers, Shangguan et al. investigate component behavior; however, they primarily focus on overall behavior and fluid–structure interaction. This paper further investigates the response of the structural components of the hydraulic mount through the use of finite strain finite elements. For clarification, the two mounts analyzed and introduced in the first paper are illustrated in Figs. 1 and 2. The finite element modeling of the structural components allows utilization of several finite element techniques such as contact analysis and large deformation shell structural analysis.

Because the majority of the structures analyzed here within consist of nearly incompressible rubber materials, hyperelastic models are required to describe their behavior. There exist many constitutive relationships designed specifically to deal with the large deformations and incompressible behavior of rubber and rubber-like materials. The majority of these relationships can be classified by three of the most common models such as the Mooney–Rivlin models, Ogden's model, and the Arruda and Boyce model [3]. All of these models rely on an expression of the strain energy density in terms of a series; therefore, the primary difficulty is not only in choosing the appropriate model, but also in finding an acceptable point to truncate the series expansion [4]. Fortunately most commercially available finite element codes have these relationships defined in various levels of truncation. For example many codes use 2, 3, 5, and 9 term expansions of the Mooney–Rivlin model [5]. This is not to say other models do not exist, several models have been introduced in efforts to better describe strain hardening effects at large strain values and others to improve compressive behaviors. Amin et al. provide a thorough description of various hyperelastic models [6]. Yet another difficulty is encountered when attempting to describe hyperelastic material properties and that is the description of material constants for the given model. Again this issue is often overcome in commercial codes via

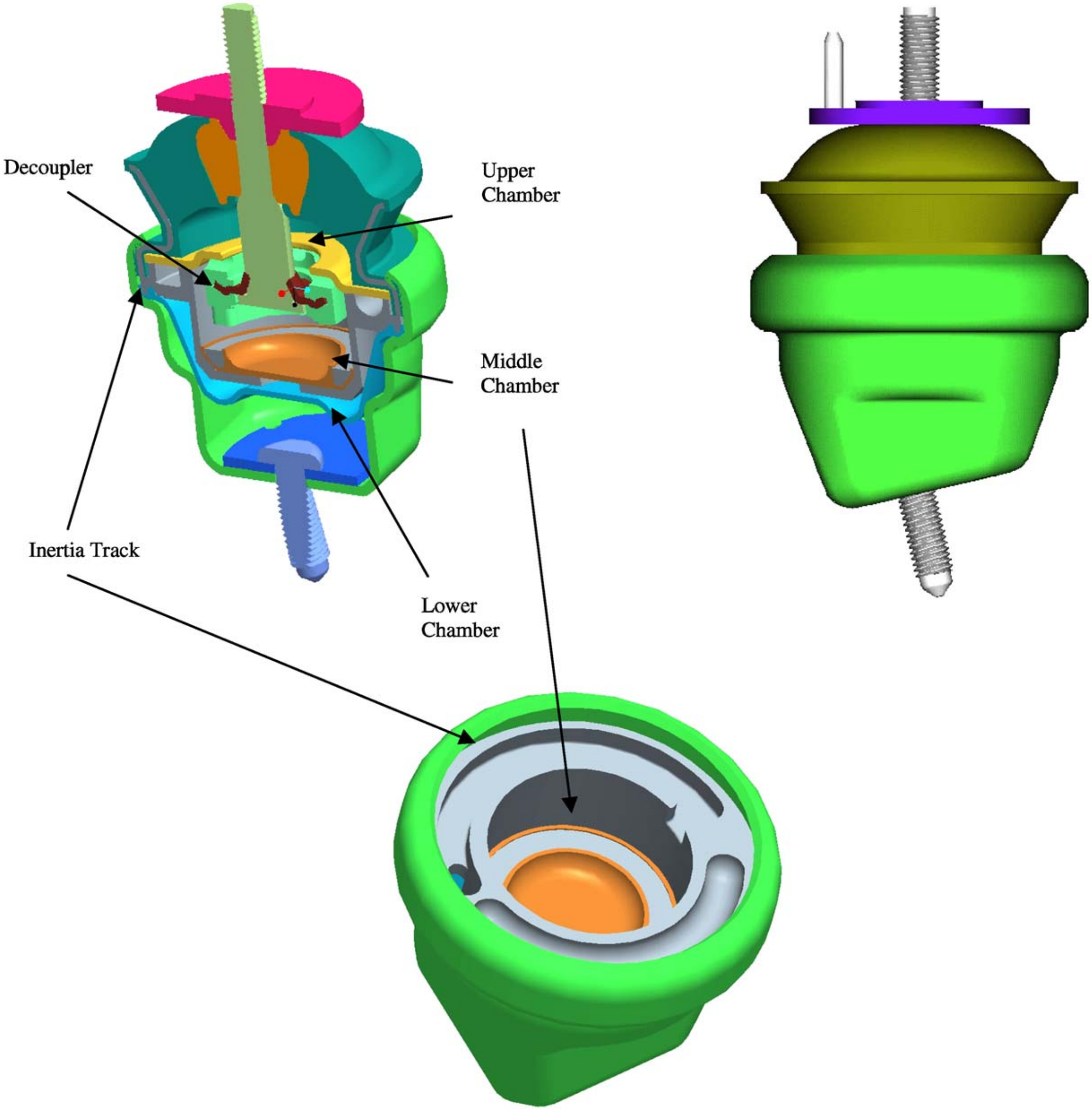

Fig. 1. Direct-decoupler hydraulic mount.

a least-squares estimation process assuming that experimental stress–strain values are available for several loading configurations [1,2].

This paper is divided into three basic components. First, the finite element model and necessary constitutive relationships are introduced. Second the boundary conditions are specified and the results analyzed, and third the frequency response equations introduced in the first paper are utilized to directly compare the behavior of the two mounts.

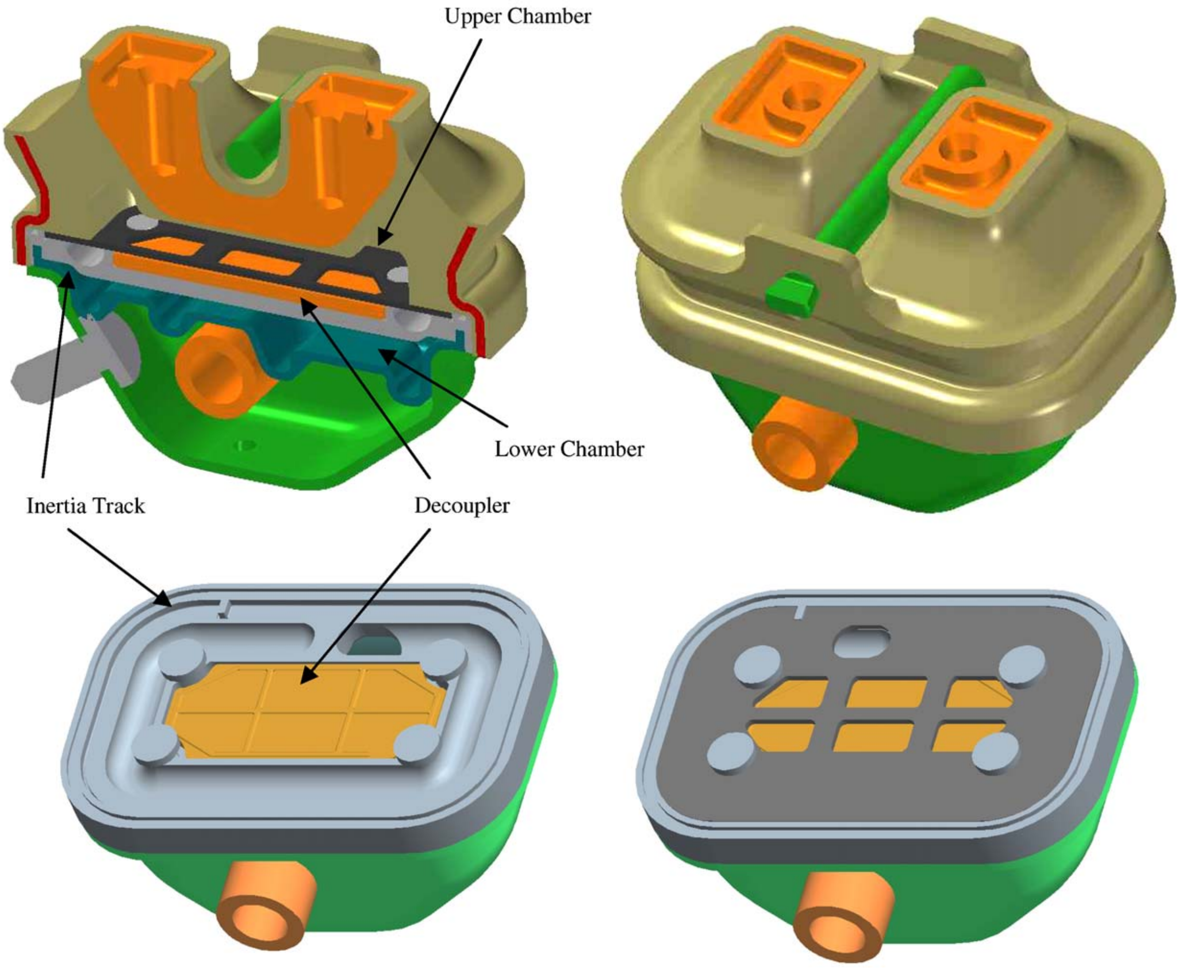

Fig. 2. Floating-decoupler hydraulic mount.

2. Component identification

The finite element model for the hydraulic engine mount centers around being able to describe the behavior of the rubber components of the hydraulic engine mount; therefore, the constitutive relationship becomes important. This analysis relies on the three term Mooney–Rivlin model to describe the rubber behavior.

$$\psi(I_1, I_2) = c_{10}(I_1 - 3) + c_{01}(I_2 - 3) + c_{11}(I_1 - 3)(I_2 - 3), \tag{1}$$

where

$$I_1 = \lambda_1^2 + \lambda_2^2 + \lambda_3^2,$$

$$I_2 = \lambda_1^2\lambda_2^2 + \lambda_2^2\lambda_3^2 + \lambda_3^2\lambda_1^2.$$

Eq. (1) represents the Mooney–Rivlin model for incompressible hyperelastic materials in terms of strain energy per unit undeformed volume. To determine the constants (c_{10}, c_{01}, and c_{11}) the model in Eq. (1) is applied and compared to experimentally obtained stress–strain data (uniaxial data is illustrated in Fig. 3) by means of a least-squares procedure [2,7,8]. Table 1 illustrates the constants obtained by applying the said methods (see also Table 2).

As shown in Fig. 3, the three-term Mooney–Rivlin model provides an exceptionally accurate fit to the experimental data beyond providing sufficient range for this analysis.

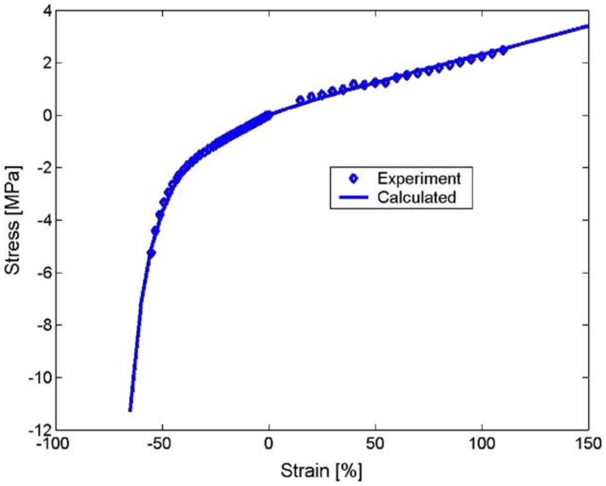

Fig. 3. Uniaxial stress–strain relationship for rubber material.

Table 1
Mooney–Rivlin model constants

Parameter	Value	Unit
c_{10}	4.838E−1	MPa
c_{01}	−9.456E−2	MPa
c_{11}	1.235E−2	MPa

Table 2
Linear elastic material properties

Material	Young's modulus	Poisson's ratio
Steel	207 GPa	0.3
Aluminum	71 GPa	0.33

3. Discretized models

3.1. Element description

The nature of the problem and the fact that the models being considered here consist of multiple materials in contact with one another emphasizes the importance of proper element selection. Much of the volume of the bodies under investigation is made from nearly incompressible rubber making hyperelastic constitutive models a necessity. However, many elements do not tolerate large deformations typically associated with hyperelastic behavior. This analysis utilized a quadratic displacement behavior element with a mixed u-P (displacement-pressure) formulation to enforce the incompressibility constraint of the material [5]. In many instances the rubber was in contact or bonded to linear-elastic-isotropic materials such as aluminum and steel. Element selection in these metallic domains was not of great concern, as excessive deformation in these regions is not expected; therefore, these domains utilized a quadratic element to ensure mesh continuity with the hyperelastic domains.

This analysis also makes use of shell elements to describe thin rubber geometries intended to exhibit large deformations. Shell elements are utilized because the geometry in question is of complex nature; however, the thickness is constant throughout the geometry. By using the shell element a higher quality mesh is obtained. With this said shell elements do have many limitations and can easily induce large errors due to spurious modes such as shear locking and the hourglass mode [9]. The element used here alters the transverse shape functions to eliminate the effect of shear locking [5]. Additional spurious modes are eliminated on the element level, and for a full description the reader is referred to Ref. [5].

3.2. Direct-decoupler mount

Fig. 4 illustrates the meshed geometry of the upper structure of the direct-decoupler mount. The model takes into account the axial symmetry of the component thereby simplifying the analysis of this component. The model consists of three distinct material domains defined by the main rubber component which acts as the main spring system of the hydraulic mount and gives the hydraulic mount the ability to support the engine. Second is the steel ring which encompasses the rubber component and provides rigidity to the rubber structure. Third is the cast aluminum domain that provides a means to connect the engine and engine mount. These differing material domains are considered perfectly bonded to one another with one exception between the rubber structure and aluminum structure (see Fig. 4). At this boundary a contact condition was specified to prevent the aluminum structure from penetrating the rubber structure as the mount deforms. The contact conditions were defined as an asymmetric contact pair utilizing a pure-penalty approach [5].

Regardless of the domain, the element used was an eight node quadrilateral element with an edge length not allowed to exceed 0.75 mm. The small element edge length allowed the use of the asymmetric contact pair model which improves computational efficiency as compared to a symmetric contact pair model [5]. In addition, the small element size was more tolerant than larger-sized elements of large structural deformations of the rubber domain of the mount thereby easing the solution and convergence processes.

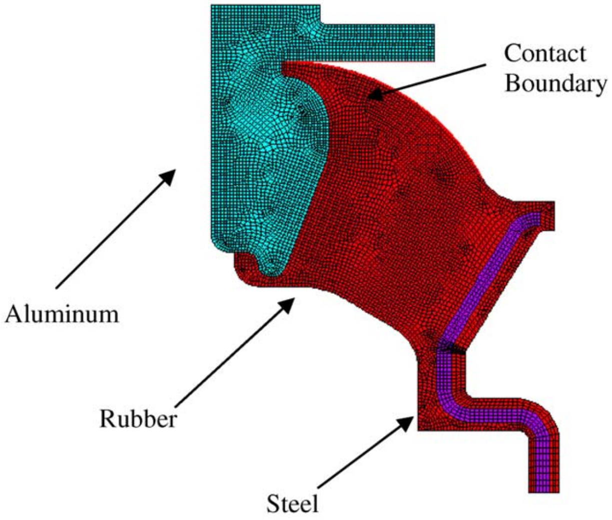

Fig. 4. Upper chamber finite element mesh (direct-decoupler mount).

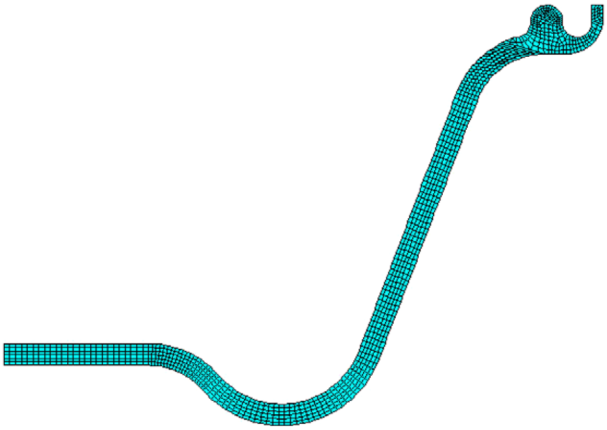

Fig. 5. Lower chamber finite element mesh (direct-decoupler mount).

Fig. 5 illustrates the meshed geometry of the lower compliance of the direct-decoupler mount. Again, as with the upper structure, axial symmetry was exploited and an eight node quadrilateral element was used. In addition, the element edge length was not allowed to exceed 0.75 mm.

Fig. 6 illustrates the meshed geometry of the middle compliance of the direct-decoupler mount. Here axial symmetry could not be exploited because of the geometry of the bottom of the compliant (see Fig. 7). The meshed geometry utilizes a 20 node hexahedral element with element edge size not allowed to exceed 2.5 mm in the aluminum body and 1 mm in the rubber domain. The model contains two distinct material domains; however, the interface between said domains is treated differently from the material interfaces in the upper structure. The interface between the

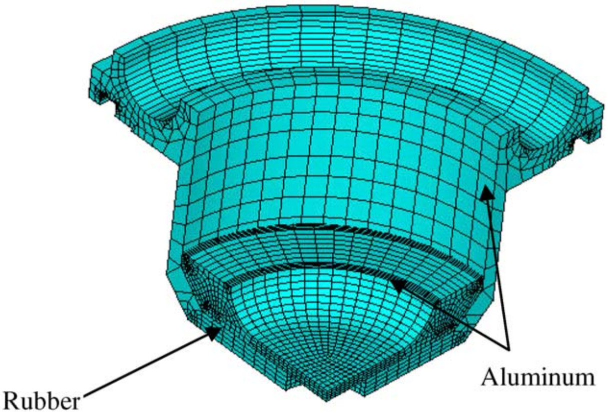

Fig. 6. Middle chamber finite element mesh (direct-decoupler mount).

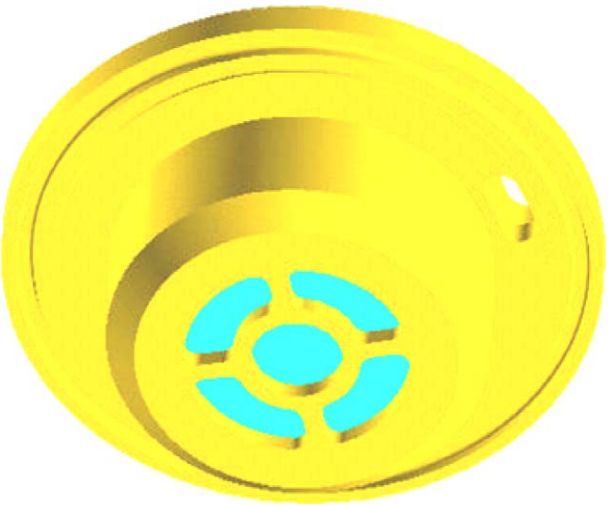

Fig. 7. Geometry of the lower surface of the middle compliance (direct-decoupler mount).

rubber and aluminum components in this model were modeled by a symmetric contact pair utilizing a pure-penalty approach. The symmetric contact was utilized as it calculates the contact condition at more points across the contact area and allows for less overlap or penetration between the contacting bodies than the asymmetric contact utilized in the upper structure analysis [5].

3.3. Floating-decoupler mount

Fig. 8 illustrates the meshed geometry of the upper structure of the floating-decoupler mount. As with the upper structure model from the direct-decoupler mount, the model of floating-

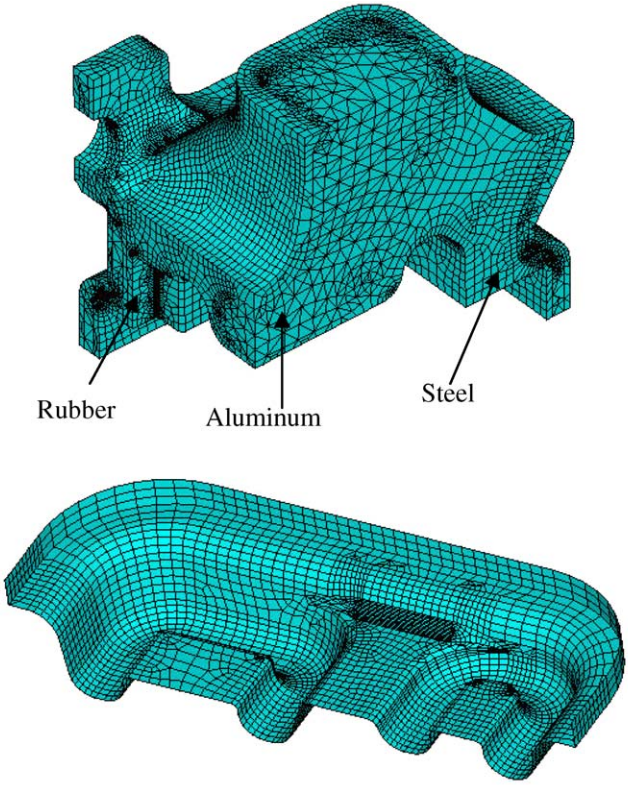

Fig. 8. Upper and lower chamber finite element mesh (floating-decoupler mount).

decoupler upper structure consists of three distinct material domains (again aluminum, rubber and steel serving the same functions as previously discussed). The material interfaces were assumed perfectly bonded to one another. This model allowed the use of symmetry conditions on two orthogonal planes thereby allowing analysis of only one quarter of the structure. To simplify the discretization process, the metallic domains were meshed using a 10 node tetrahedral element that was deemed suitable noting the relatively small strains incurred in these domains as compared to the rubber domain. The rubber domain was meshed using a 20 node hexahedral element with an edge size not allowed to exceed 2 mm to better accommodate the large strains inherent in this domain. The transition region between the dissimilar meshes was meshed using a 13 node pyramid element within the metallic domains. The tension pin was not included in the model as a means to simplify the analysis as it was assumed to only provide support to large tensile-load-induced deformations.

Fig. 8 illustrates the meshed geometry of the lower compliance from the floating-decoupler mount. Because this domain was constant in thickness throughout the model was discretized along its mid-plane using four node shell elements with edge length not exceeding 1 mm. The shell element uses the Mindlin–Reissner formulation and an altered shape functions to help avoid shear locking-type phenomenon inherent in shell elements [3,5].

4. Boundary conditions

4.1. Direct-decoupler mount

Fig. 9 illustrates the boundary conditions of the finite element model for the upper structure from the direct-decoupler mount. For the case where the load–deflection characterizes, a pressure was applied to the upper surface of the aluminum structure as shown in Fig. 9. In addition, the mount was fixed from motion at the location where it mates with the remainder of the mount. Thirdly, the mount was constrained from any possible axial motion by providing such constraints along the axis of symmetry. To analyze the mount for volumetric compliance the pressure applied on the upper surface was removed and a pressure was placed across the inner surface as shown in Fig. 9 to simulate the pressure induced by the fluid.

Fig. 10 illustrates the boundary conditions for the lower chamber from the direct-decoupler mount. As with the upper structure model this model fixes all displacement degrees of freedom associated with the surfaces that contact the remainder of the engine mount. Load is applied as an evenly distributed pressure across the internal surface of the geometry to simulate the pressure applied by the fluid. Along the axis of symmetry radial displacement constraints are also instituted to ensure no inappropriate deformations.

Fig. 11 illustrates a cross section of the middle chamber from the direct-decoupler mount to better illustrate the boundary conditions. As with previous models the interface between the middle chamber and the remainder of the mount was fixed in all displacement degrees of freedom. In addition, an evenly distributed pressure was applied to the inner surfaces of the middle chamber to simulate the fluid induced pressure. Also, a displacement constraint in all degrees of freedom was applied to the upper surface of the aluminum structure in the interior of the middle chamber as to simulate a retaining clip used in the actual mount (not modeled). Symmetry displacement conditions were also applied to the two planes of symmetry for this model (see Fig. 6).

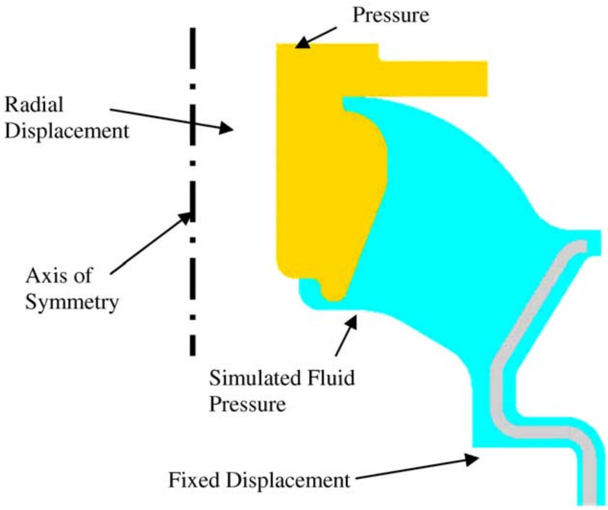

Fig. 9. Upper chamber boundary conditions (direct-decoupler mount).

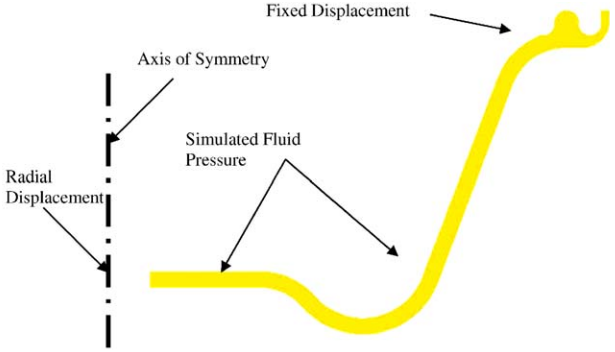

Fig. 10. Lower compliance boundary conditions (direct-decoupler mount).

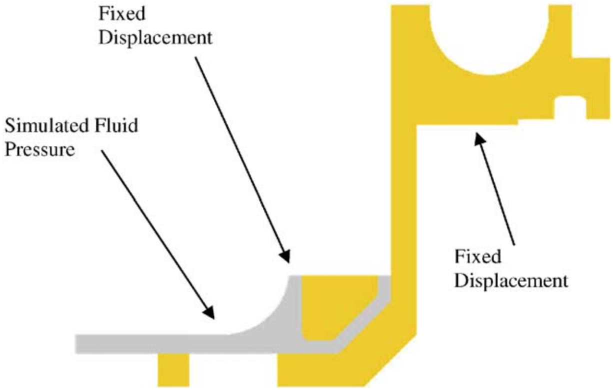

Fig. 11. Middle compliance boundary conditions (direct-decoupler mount) (cross section shown for better illustration).

4.2. Floating-decoupler mount

Fig. 12 illustrates the boundary conditions enforced upon the upper structure of the floating-decoupler mount. Because of the geometry the structure was quartered and symmetry displacement conditions were applied to each plane of symmetry. To ascertain the load–deflection behavior of the structure a pressure load was applied to the upper surface of the aluminum structure of the mount. In addition, at locations where the upper structure joins to the remainder of the mount displacement constraints were assigned in all degrees of freedom. For analysis of the volumetric compliance, a pressure was applied in an even manner across all surfaces exposed directly to fluid when the mount is in an assembled configuration (this pressure was not applied when analyzing the load–deflection behavior).

Fig. 13 illustrates the boundary conditions applied to the lower compliance of the floating-decoupler mount. Here, symmetry displacement and rotation constraints were instituted along the plane of symmetry. As in previous models the portions of the geometry that joined the remainder of the mount were fixed from motion in all degrees of freedom and fluid pressure was simulated by

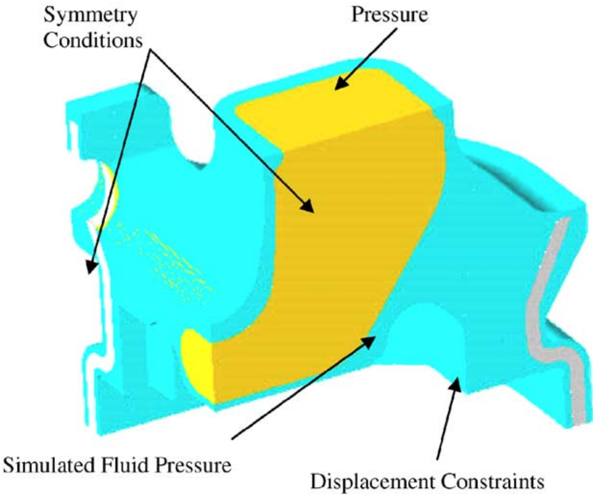

Fig. 12. Upper chamber boundary conditions (floating-decoupler mount).

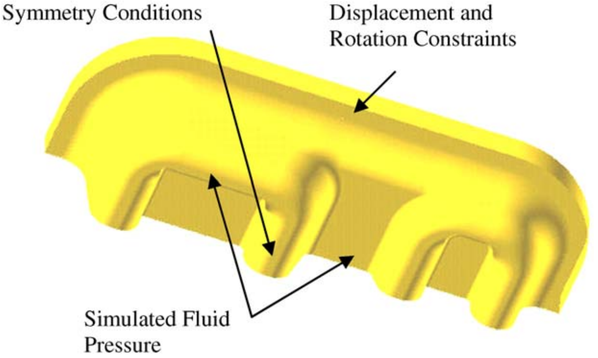

Fig. 13. Lower compliance boundary conditions (floating-decoupler mount).

applying an evenly distributed pressure across all surfaces directly exposed to fluid while the mount is in an assembled configuration.

5. Parameter identification

5.1. Direct-decoupler mount

Fig. 14 illustrates the load–deflection relationship obtained from the finite element model of the upper structure of the direct-decoupler mount. In addition, a simple experiment was run to verify the finite element model with the results illustrated as a comparison in Fig. 14.

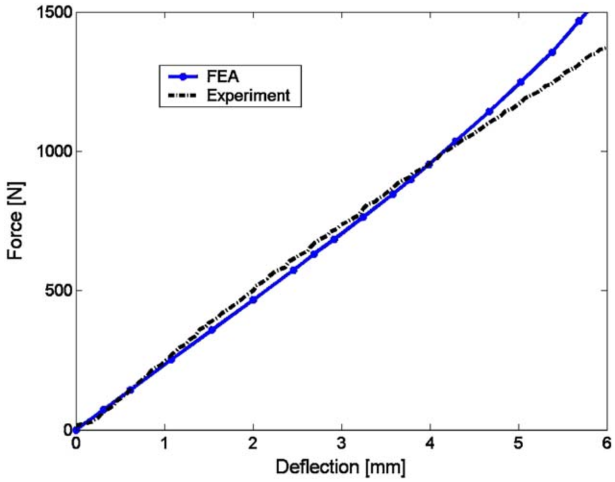

Fig. 14. Force-deflection relationship (direct-decoupler mount).

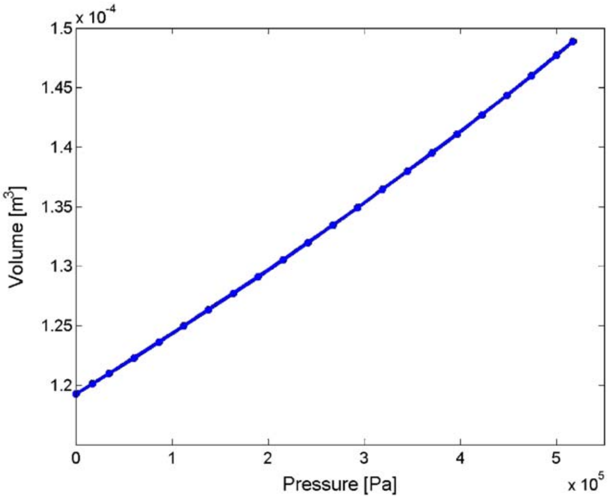

Fig. 15. Upper chamber volume–pressure relationship (direct-decoupler mount).

Because the load–deflection relationship is approximately linear an equivalent stiffness value may be defined as the mean slope of the load–deflection curve. Experimental results indicate a stiffness value of 230.9 N/mm whereas finite element results indicate a stiffness value of 235.4 N/mm (~1.9% difference). Because of the excellent agreement between the finite element model and experiment the finite element models are considered sufficiently accurate for this investigation.

Fig. 15 illustrates the finite element results calculating the change in volume enclosed by the structure as compared to the applied pressure. In order to calculate the volume at a specific load

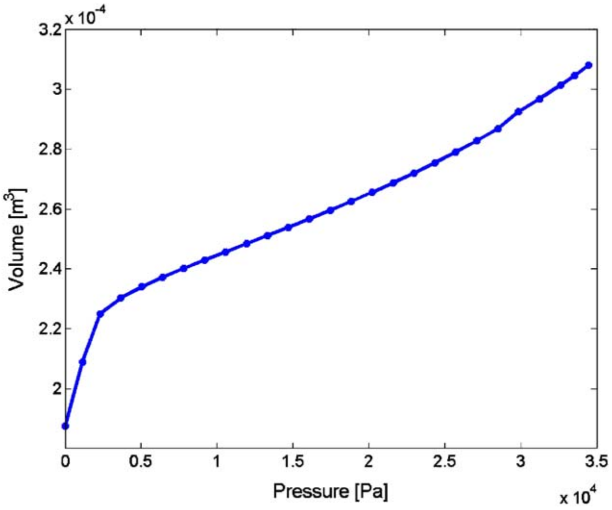

Fig. 16. Lower chamber volume–pressure relationship (direct-decoupler mount).

step a trapezoidal numerical integration routine was used to approximate the volume integral. The slope of the line in Fig. 15 yields the volumetric compliance of the upper structure. Utilizing the mean slope of the line again noting the lines approximate linearity yields a compliance value of 5.70E−11 m^5/N.

Fig. 16 illustrates the enclosed volume as compared to applied pressure relationship for the lower compliance of the direct-decoupler mount. Notice that this curve is highly nonlinear; therefore, linearization about an operating point is required, and allowing the operating point to exist beyond 5 kPa yields a volumetric compliance of 2.624E−9 m^5/N. Utilizing an operating point above 5 kPa is acceptable noting that the static mount pressure is higher than said value.

Fig. 17 illustrates the volume–pressure relationship obtained from the finite element model of the middle chamber of the direct-decoupler mount. Utilizing the slope of the curve gives a mean volumetric compliance of 2.923E−11 m^5/N.

5.2. Floating-decoupler mount

Fig. 18 illustrates the load–deflection relationship obtained for the upper structure of the floating-decoupler mount by the finite element model and experimentally. The finite element model yields an equivalent stiffness value of 558.28 N/mm whereas the experiment yields an equivalent stiffness value of 531.06 N/mm, a 4.8% difference illustrates the effectiveness of the finite element model.

Fig. 19 illustrates the volume–pressure relationship for the upper-structure of the floating-decoupler mount. Noting the approximate linearity of the relationship illustrated in Fig. 19 the mean slope of the curve yields a volumetric compliance of 5.118E−11 m^5/N.

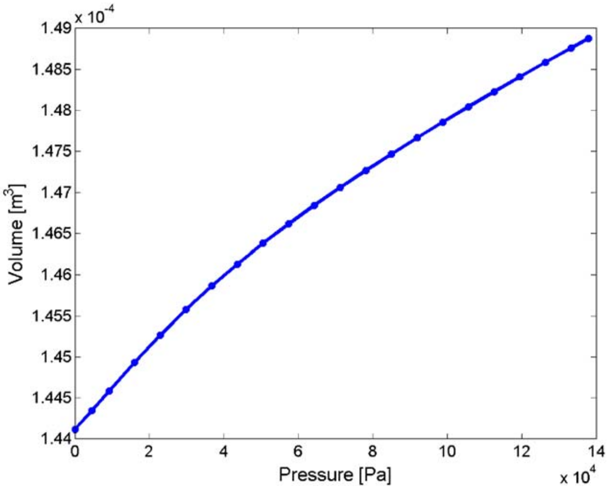

Fig. 17. Middle chamber volume–pressure relationship (direct-decoupler mount).

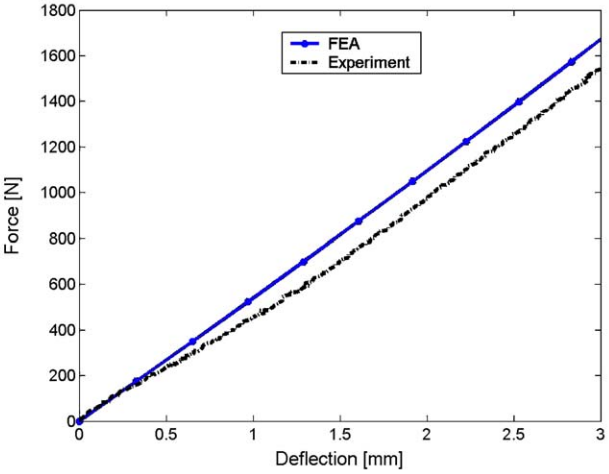

Fig. 18. Force-deflection relationship (floating-decoupler mount).

Fig. 20 illustrates the volume–pressure relationship from the lower chamber of the floating-decoupler mount. Assuming an operating pressure above 10 kPa yields an average linearized compliance value of 2.85E−9 m^5/N.

Table 3 illustrates the parameter values for the two hydraulic mounts analyzed as calculated from the finite element models and direct measurement from the mounts. Adiguna et al. describe methods to obtain the fluid damping and equivalent mass properties for the fluid passages, and this analysis uses the capillary tube formula discussed there within [10].

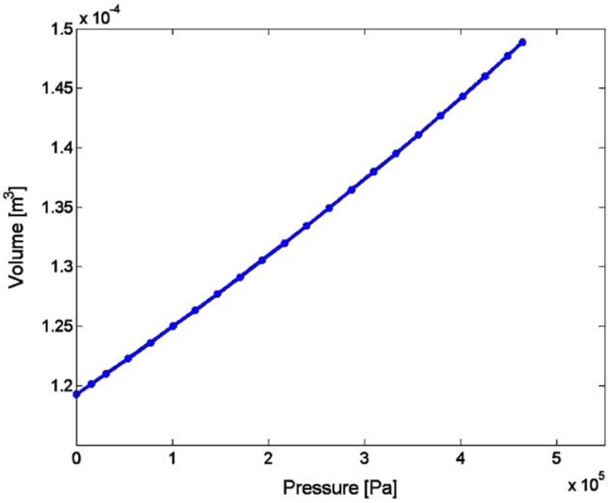

Fig. 19. Upper chamber volume–pressure relationship (floating-decoupler mount).

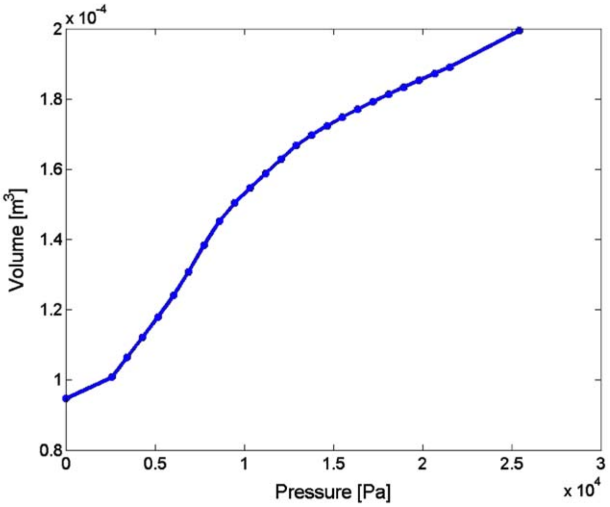

Fig. 20. Lower chamber volume–pressure relationship (floating-decoupler mount).

6. Frequency responses

From the first paper the nonlinear equations of motion for the floating-decoupler mount and direct-decoupler mount are, respectively

$$\begin{bmatrix} M_d & 0 \\ 0 & M_i \end{bmatrix} \begin{Bmatrix} \ddot{x}_d \\ \ddot{x}_i \end{Bmatrix} + \begin{bmatrix} B_d & 0 \\ 0 & B_i \end{bmatrix} \begin{Bmatrix} \dot{x}_d \\ \dot{x}_i \end{Bmatrix} + \begin{bmatrix} A_d^2 K & A_d A_i K \\ A_d A_i K & A_i^2 K \end{bmatrix} \begin{Bmatrix} x_d \\ x_i \end{Bmatrix} + F_{\mathrm{fd}} \begin{Bmatrix} 1 \\ 0 \end{Bmatrix} = \frac{A_p}{C_1} \begin{Bmatrix} A_d \\ A_i \end{Bmatrix} x, \tag{2}$$

Table 3
Values for hydraulic mount

Symbol	Floating-decoupler	Direct-decoupler	Unit
A_i	4.297E−05	6.668E−05	m^2
A_d	5.303E−05	8.107E−05	m^2
A_p	5.345E−03	3.663E−03	m^2
A_B	—	2.027E−03	m^2
B_i	2.409E−02	2.852E−03	Ns/m
B_d	1.031E−04	2.140E−01	Ns/m
B_r	0.500E+03	0.500E+03	Ns/m
C_1	5.118E−11	5.700E−11	m^5/N
C_2	2.850E−09	2.923E−11	m^5/N
C_3	—	2.624E−09	m^5/N
K	1.989E+10	5.214E+10	N/m^5
K_r	5.583E+05	2.354E+05	N/m
M_i	9.887E−03	1.773E−03	kg
M_d	5.220E−04	1.643E−03	kg
E	0.5	0.5	—
Δ	5.000E−04	4.500E−03	m
X	1.0E−3	1.0E−3	m

Table 4
Linear model natural frequency comparison

	f_1 (Hz)	f_2 (Hz)
Floating-decoupler	85.48	0
Direct-decoupler	82.96	23.95

$$\begin{bmatrix} M_d & 0 \\ 0 & M_i \end{bmatrix} \begin{Bmatrix} \ddot{x}_d \\ \ddot{x}_i \end{Bmatrix} + \begin{bmatrix} B_d & 0 \\ 0 & B_i \end{bmatrix} \begin{Bmatrix} \dot{x}_d \\ \dot{x}_i \end{Bmatrix} + \begin{bmatrix} A_d^2 K & -\dfrac{A_d A_i}{C_2} \\ -\dfrac{A_d A_i}{C_2} & \dfrac{A_i^2}{C_2} \end{bmatrix} \begin{Bmatrix} x_d \\ x_i \end{Bmatrix} + F_{\mathrm{dd}} \begin{Bmatrix} 1 \\ 0 \end{Bmatrix} = \begin{Bmatrix} A_d \left(\dfrac{A_p}{C_1} - A_B K \right) \\ \dfrac{A_i A_B}{C_2} \end{Bmatrix} x. \tag{3}$$

Using the linearized version, assuming an open decoupler, of the equations of motion illustrated in (2) and (3) yields the natural frequency values listed in Table 4.

Note that the floating-decoupler mount exhibits a zero natural frequency for one degree of freedom. This corresponds to the shortcircuiting of the inertia track from the system noting the decoupler is never allowed to close in the linear model, and therefore provides the most efficient means of pressure equalization across the two fluid chambers. The direct-decoupler mount does not exhibit such behavior noting that its inertia track is forced into service because the decoupler and inertia track are in series.

The frequency response functions obtained in the first paper by utilization of the method of averaging are expressed for convenience here in Eqs. (4)–(7).

$$K_{\mathrm{dyn}} = \frac{1}{X}\sqrt{X\left(K_r G_1 + B_r \omega G_2 + A_p^2 p_1^2\right)}, \tag{4}$$

$$\phi_{\mathrm{sys}} = \arctan\left(\frac{B_r X\omega + A_p p_1 \sin(\phi_1)}{K_r X + A_p p_1 \cos(\phi_1)}\right), \tag{5}$$

$$K_{\mathrm{dyn}} = \frac{1}{X}\sqrt{(B_r X\omega)^2 - 2B_r X\omega S_1 + (K_r X)^2 - 2K_r X S_2 - A_B^2 S_3 + 2A_B A_p p_1 S_4 + (A_p p_1)^2}, \tag{6}$$

$$\phi_{\mathrm{sys}} = \arctan\left(\frac{B_r X\omega - S_1}{K_r X - S_2}\right). \tag{7}$$

Eqs. (4) and (5) refer to the floating-decoupler mount whereas Eqs. (6) and (7) refer to the direct-decoupler mount. Both systems of equations are fully defined in the first paper and presented here solely for reference.

Figs. 21 and 22 illustrate the results of Eqs. (4)–(7) using the mount parameters determined via the finite element models. Fig. 21 illustrates a comparison between the two mounts dynamic stiffness responses normalized by their respective static upper structure stiffness values (K_r). As is readily apparent by the dynamic stiffness curves and phase lag curves the direct-decoupler mount

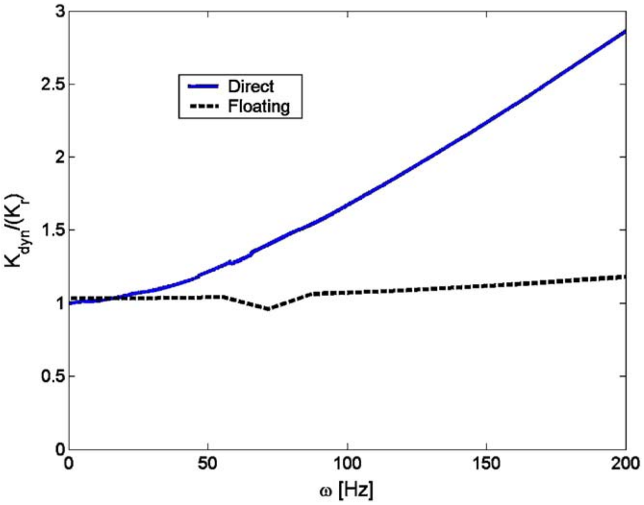

Fig. 21. Dynamic stiffness comparison plot.

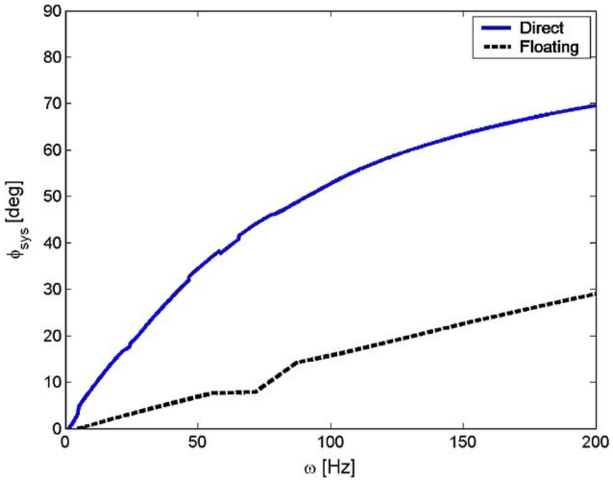

Fig. 22. System phase lag comparison plot.

exhibits characteristics of over damping as compared to the floating-decoupler mount and is incapable of providing the appropriate switching mechanism to alleviate the high damping at increased frequencies. However, the floating-decoupler mount appears to provide sufficient damping through primary resonance and then appears to provide a substantial decrease in damping as witnessed in the frequency response curves in Figs. 21 and 22. More specifically, the rate of increase of the frequency response function describing the floating-decoupler mount is significantly less than that of the direct-decoupler mount indicating the floating-decoupler mount exhibits a significantly lower damping coefficient than that of the direct-decoupler. In addition, the phase lag of the floating-decoupler mount is substantially less than that of the direct-decoupler mount thereby indicating a significant difference in the overall system damping.

7. Conclusions

It has been illustrated that finite element analysis provides an accurate and highly effective method in parameter identification to aid in the design process of such devices. In addition, the accuracy of the finite element analysis as compared to experiment for describing rubber material incompressible behavior characteristics has been verified on a practical example. Along with using the finite element models, the lumped parameter modeling introduced in the first paper and extended here is appropriate and effective for describing the nonlinear behavior of hydraulic mounts in a frequency domain thereby presenting an attractive, efficient and effective tool for design and analysis of nonlinear suspensions. In addition to illustrating that nonlinear finite elements are effective as a design tool for hydraulic mounts the superiority of the floating-decoupler mount design in isolating vibration and providing a means of frequency dependent damping has been illustrated noting that for the system to exhibit a frequency dependent damping characteristic the switching mechanism must be decoupled from the actual input excitation of the system and allowed to react to the behavior of the system as a whole.

References

[1] W.B. ShannggGuan, Z.H. Lu, Modelling of a hydraulic engine mount with fluid-structure interaction finite element analysis, *Journal of Sound and Vibration* 275 (1–2) (2004) 193–221.

[2] W.B. Shangguan, Z.H. Lu, Experimental study and simulation of a hydraulic engine mount with fully coupled fluid-structure interaction finite element analysis model, *Journal of Computers and Structures* 82 (2004) 1751–1771.

[3] T. Belytschko, W.K. Liu, B. Moran, *Nonlinear Finite Elements for Continua and Structures*, Wiley, New York, 2000.

[4] A. Duster, S. Harmann, E. Rank, p-FEM Applied to finite isotropic hyperelastic bodies, *Journal of Computational Methods In Applied Mechanics and Engineering* 192 (2003) 5147–5166.

[5] SAS IP, Inc., ANSYS 8.0 Help Documentation, 2003.

[6] A.F.M.S. Amin, M.S. Alam, Y. Okui, An improved hyperelasticity relation in modeling viscoelasticity response of natural and high damping rubbers in compression: experiments, parameter identification and numerical verification, *Journal of Mechanics of Materials* 34 (2002) 75–95.

[7] D.J. Charlton, Y. Yang, K.K. Teh, A review of methods to characterize rubber elastic behavior for use in finite element analysis, *Rubber Chemistry and Technology* 67 (2000) 481–503.

[8] D.J. Seibert, N. Schoche, Direct comparison of some recent rubber elasticity models, *Rubber Chemistry and Technology* 73 (2000) 366–384.

[9] L.A. Duarte Filho, M.A. Awruch, Geometrically nonlinear static and dynamic analysis of shells and plates using the eight-node hexahedral element with one-point quadrature, *Journal of Finite Elements in Analysis and Design* 40 (2004) 1297–1315.

[10] H. Adiguna, M. Tiwari, R. Singh, H.E. Tseng, D. Hrovat, Transient response of a hydraulic engine mount, *Journal of Sound and Vibration* 268 (2003) 217–248.